Original Article

Improvement of tensile properties by controlling the microstructure and crystallographic data in commercial pearlitic carbon-silicon steel via quenching and partitioning (Q&P) process

M.A. Mohtadi-Bonab [a,], Edwan A. Ariza [b,c], Rodrigo C.P. Loureiro [d], Dany Centeno [b], Felipe M. Carvalho [e], Julian A. Avila [f,h], Mohammad Masoumi [g,**]*

[a] *Department of Mechanical Engineering, University of Bonab, Bonab, Iran*

[b] *Escuela de Tecnología Mecánica, Universidad Tecnológica de Pereira, Carrera 27 #10-02 Alamos, Pereira, 660003, Colombia*

[c] *Metallurgical and Materials Engineering Department, University of São Paulo, Av. Prof. Mello Moraes, 2463, São Paulo, Brazil*

[d] *Materials Characterization Laboratory (LACAM), Department of Metallurgical and Materials Engineering, Federal University of Ceará, Campus Do Pici, Fortaleza Ceará, Brazil*

[e] *Metallurgical Processes Laboratory, Institute for Technological Research, Av. Prof. Almeida Prado, 532 São Paulo, Brazil*

[f] *Department of Strength of Materials and Structural Engineering, Barcelona School of Engineering (ETSEIB), Universitat Politècnica de Catalunya, Barcelona, Spain*

[g] *Centro de Engenharia, Modelagem e Ciências Sociais Aplicadas, Universidade Federal Do ABC, 09210-580, Santo André, SP, Brazil*

[h] *Department of Aeronautical Engineering, School of Engineering of São João (FESJ) São Paulo State University, São João da Boa Vista, SP, Brazil*

ARTICLE INFO

ABSTRACT

In the current research, a complex microstructure and crystallographic data were developed through quenching and partitioning (Q&P) process to improve tensile properties of commercial pearlitic carbon-silicon steel. Two-stage Q&P process, including full austenitization, quenching at 220 °C, followed by two different partitioning temperatures, was applied to the as-received specimen to generate a complex microstructure composed of tempered martensite, bainite, ultrafine carbides/martensite-austenite/retained austenite particles. Microstructure and crystallographic data were investigated by scanning electron microscopy, electron backscattered diffraction (EBSD), and X-ray diffraction techniques. Then, hardness and tensile properties were evaluated to confirm the improvement of mechanical properties. Dilatation-temperature curves exhibited the kinetics of martensitic and bainitic transformation during quenching and isothermal partitioning stages. The

---

* Corresponding author.
** Corresponding author.
   E-mail addresses: m.mohtadi@ubonab.ac.ir (M.A. Mohtadi-Bonab), mohammad.m@ufabc.edu.br (M. Masoumi).

presence of nano-carbide particles inside athermal martensite was confirmed by electron microscopy due to the pre-formed martensite carbon depletion during the partitioning stage coupled with bainitic transformation. The formation of preferential atomic-compact <111> direction in BCC (martensite/bainite) plates characterized by EBSD, could enhance ductility by providing adequate slip systems. Point-to-point misorientation analyses demonstrated a slight dominance of low angle boundaries proportion in bainitic dominance structure in Q&P-220-375 specimen, which could be used in phase characterization. Results revealed that the development of nanoscale carbide dispersed in refined bainite/martensite matrix boosted the yield and ultimate tensile strength by over 100% and 110% compared to the initial pearlitic microstructure. However, ductility reduced to half value in Q&P-220-325 and Q&P-220-375 specimens.

1. Introduction

The demand for steels with high strength, low weight and improved ductility has been recently increased in the last several decades. The processing of steel with special heat treatments helps industry to reach these goals. Quenching and partitioning (Q&P) is used as one the novel heat treatments in order to produce martensite, bainite, and high fraction of retained austenite in the microstructure of steels [1]. In this regard, Speer et al. [2] used a special heat treatment, named as "quenching and partitioning" to increase the strength of steel without reducing the ductility by producing the steel with the microstructure of martensite coupled with high fraction of retained austenite. It is worth-mentioning that the retained austenite is expected to improve the mechanical properties of steel by increasing the ductility and toughness of the material due to the transformation induced plasticity (TRIP) effect [3]. In order to do quenching and partitioning, the steel specimen is heated to an austenitizing temperature above the A_{c3} or between the A_{c1} and A_{c3} to do complete or partial austenitization, respectively. After the austenitization, the specimen is quenched to a temperature between the martensite start temperature (M_s) and finish transformation temperature (M_f) in order to form carbon saturated martensite. After quenching, a partitioning is carried out by maintaining the temperature at the quenching temperature for a longer time or by increasing the temperature to partitioning temperature which close to the M_s. At the end, the steel material is quenched to room temperature [3]. The partitioning step is carried out in order to increase the carbon atoms migration from the carbon-saturated martensite to the surrounded untransformed austenite. It is notable that the stability of the untransformed austenite is increased during the partitioning process at room temperature since the transformation of the austenite to fresh martensite during the final quenching step is minimized or suppressed [4,5].

In this research, commercial carbon-silicon C–Si steel with original pearlitic structure was selected to study the effect of complex microstructures and crystallographic data evolution on mechanical properties. Because they are very important in the industry due to their high strength and good ductility and are widely used in various industries. These high mechanical properties depend mainly on the cementite alignment, the cementite interlamellar spacing, and desirable crystallographic texture of the ferritic matrix [6,7]. Two important parameters play a key role in microstructural parameters including the pearlite interlamellar spacing and thickness of cementite lamellae. These parameters are controlled by thermomechanical processing and microalloying [8]. Many obstacles for dislocation glide prevent strain localization at ferrite-cementite interfaces which provides good ductility in pearlitic steels. Addition of microalloying elements and control of cooling rate are considered as important methods to produce the fine ferrite-cementite lamellar structure. It is worth-mentioning that cementite particles with spheroidal shape improve the work hardening ability of hypereutectoid steels [9–14].

The mechanical properties and hardness of a steel strongly depends strongly on its microstructure and crystallographic orientation, and boundary conditions. Due to this importance, numerous studies in the literature have focused on the microstructure and texture evolution in different types of steels [15–20]. Masoumi et al. [15] reported the improvement of wear resistance and mechanical performance of hypereutectoid pearlitic steel under an interrupted quenching from full austenitization temperature and subsequent partitioning step in the range of 350–650 °C. This process was carried out to set multicomponent structure consisting of tempered martensite, bainite, retained austenite, and pearlite colonies. Dong et al. [16] developed nano-bainite structures accompanied by film-like retained austenite through conventional one- and two-stage Q&P processes to improve work hardening. Guo et al. [17] investigated the influence of the quenching step on subsequent bainitic transformation kinetic on two-stage Q&P, reporting a 23% improvement for ultimate tensile strength compared with traditional bainitic isothermal transformation. Hosseini et al. [18] reported the carbon enrichment of austenite at 280–400 °C coupled with carbon depletion from martensite in a medium carbon steel (0.6C-1.6Si-1.25Mn-1.75Cr wt%). Singh et al. [20] modeled the effect of high silicon content on the kinetics of bainite plates, where silicon suppresses the carbide precipitation, resulting in refined bainite plates. Although a large amount of efforts has been conducted on specially designed chemical compositions of steel to set nanostructured carbide-free bainite

to maximize their mechanical properties, a few researches [21–24] have been carried out on commercially available steel grades such as commercially-available C—Si steel. CruzJunior et al. [21] investigated the effect of isothermal treatment temperature and tempering of a spring steel. The complex microstructure containing tempered martensite, ferritic-bainite, retained austenite films, and carbides was developed under isothermally treated at 200 °C followed by tempering at 400 °C for 1 h. Although the similar mechanical properties were obtained independent from isothermal treatment times, yield and ultimate tensile strength decreased with increasing isothermal treatment temperature, due to a lower volume fraction of martensite formed in the initial cooling. Then, the values of energy absorbed drastically decreased by tempering at higher temperatures due to the decomposition of retained austenite blocks into bainite rich in carbides. They also documented that ferritic-bainite laths can be produced by transformation at low temperatures, resulting in enhanced mechanical properties of martensitic steels and increased resistance to tempering [22]. Bainite was the predominant phase in the microstructure in the specimens tempered at 400 °C due to the decomposition of the retained austenite blocks. Moreover, the bainite transformation without carbide precipitation partitions the carbon to the austenite, which later decomposes during tempering observed just above the martensite start temperature. Santos et al. [23] also studied the influence of austempering on the mechanical behavior of a spring steel 0.56C-1.43Si-0.58Mn-0.47Cr (wt. %), with TRIP effect. The excellent combination of strength and ductility was achieved by treating at 220 °C, since a mixture of martensite and very fine ferritic-bainite with interlath film of retained austenite was formed. Serbino et al. [24] compared the fatigue behavior of quenched/tempered consisted of tempered martensite and austempered predominantly lower bainite of a Fe-0.55C-1.34Si-0.72Mn-0.71Cr (wt %) high strength steels. Lower bainite with some retained austenite, but without precipitated carbides at grain boundaries performed better at the highest stress amplitude (500 MPa), resulting in higher total fatigue life.

In this study, the effect of the two-stage Q&P process on microstructure and crystallographic data was studied on commercial carbon-silicon steel in order to improve mechanical properties by a set of desirable complex microstructures. Dilatation-temperature curves were tracked to understand phase transformation kinetics during quenching and isothermal partitioning stages. Then, the resulting complex microstructures (including tempered martensite, ferritic-bainite laths, retained austenite, and martensite/austenite particles) were characterized by scanning electron microscopy (SEM). Then, crystallographic data evolution such as crystal orientation, boundary conditions, and activated slip systems was investigated by electron backscattered diffraction technique. Variations of critical nucleus size, defect density, and c/a ratio were then calculated from the corresponding XRD pattern of the investigated samples. Finally, nanoindentation and tensile tests were carried out to evaluate the influence of the designed Q&P multicomponent structure on the mechanical properties of commercial steel with 1.56 wt % silicon content.

2.   Experimental procedure

All experiments were carried out on a commercial pearlitic carbon-silicon steel with the chemical composition as shown in Table 1. The steel was subjected to Q&P treatments using high precision Bahr DIL 805 A dilatometer with fused silica rod as a reference and pure Ar gas for quenching medium. Fig. 1 shows the schematic illustration of the experiment process. Cylindrical as-received C—Si steel specimens (4 mm diameter with 10 mm length) were heated with the rate of 20 °C/S until the temperature reaches 850 °C. Then, the specimens were austenitized at 850 °C for 180 s. When the austenitization is completed, specimens were cooled with the rate of 80 °C/S until the temperature of 220 °C below martensite start temperature. At this temperature, specimens were heated again with the rate of 20 °C/S until the temperatures of 325 °C and 375 °C are achieved for two specimens, called partitioning. It is worth-mentioning that the partitioning period for specimens differs in investigated specimens due to the kinetics of bainitic transformation. When the partitioning temperature is increased, the carbide particles may nucleate and grow, making the steel fragile. Therefore, in order to avoid brittleness in Q&P-220-375 specimen which is partitioned at a higher temperature, the partitioning time is reduced to the half of the partitioning time of the first specimen (Q&P-220-325). At the end, both specimens were cooled with the rate of 80 °C/S until ambient temperature.

The detailed microstructural investigation was carried out using scanning electron microscopy (SEM, FEI-Inspect F50). Metallographic specimens were prepared by mechanical grinding using SiC paper up to 1200, followed by polishing with diamond paste (6, 3, and 1 μm), and etching in 3% Nital for approximately 30 s. Microstructural constituents were observed with secondary electron images of SEM with an accelerating voltage of 20 kV and a working distance of 10 mm. The microhardness was then measured using a Shimadzu (HMV-2TADW) microhardness tester with 9.807 N of load for 15 s (HV1). The reported microhardness values are the average from 10 indentations. Nanoindentation test was conducted to investigate the mechanical performance of resulting multiphase treated samples. Nanoindentation was carried out by applying a force of 3 mN using a Berkovich type indenter on Triboindenter TI 950 (Hysitron Inc.). The load−displacement data then collected. EBSD measurements were done on an FEI-Inspect F50 SEM equipped with a field emission gun (FEG) and EBSD detector. Before the EBSD measurements, the specimens were prepared according to the standard preparation and polished with 50 nm colloidal silica slurry for 3 h. All analyses were carried out with an accelerating voltage of 20 kV, a spot size of 75 nm, a working distance of about 12 ± 2 mm, and a step size of 25 nm with hexagonal scan grid mode. The EBSD and crystallographic data were analyzed

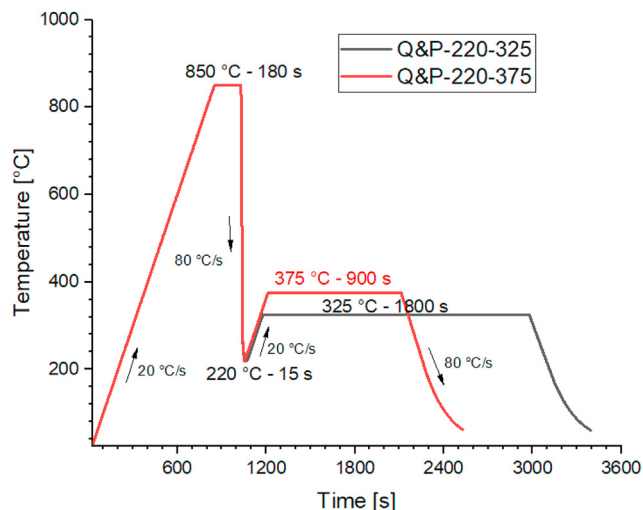| Table 1 − Chemical composition of commercial C−Si steel (wt.%).			
C	Si	Mn	Cr
0.55	1.56	1.52	0.02

Fig. 1 – Schematic illustration of the experiment process including austenization at 850 °C, quenching at 220 °C, following partitioning at 325 °C and 375 °C, and final quenching.

Fig. 2 – SEM micrograph of the microstructure of the original as-received pearlitic steel.

using TSL OIM data analysis 7 and ATEX [25]. X-ray diffraction was carried out on un-etched specimens, after polishing to 6 μm, using an X-pert PRO diffractometer with filtered Cu_K_α radiation. A continuous scanning mode was made over the angular width $2\theta = 30-120°$, with 0.02° angle step and collecting time of 2 s at each step. The XRD patterns then analyzed by Multiple Whole Profile (MWP) mathematical methods, proposed by Dragomir et al. [26]. Finally, room temperature uniaxial tensile tests were performed using an Instron model 3369 testing machine on subsized dilatometry specimens (gauge length of 4.0 mm, overall length of 10.0 mm and thickness of 1.5 mm). Engineering stress–strain data was reported from the average of three tensile specimens at a strain rate of 2×10^{-3} s^{-1}.

3. Results and discussion

Fig. 2 shows the SEM image of the microstructure of the as-received hot-rolled pearlitic steel. As seen in this image, the microstructure of as-received steel is fully composed of fine pearlite microstructure. In this image, the ferrite and cementite phases are shown by dark and bright colors respectively. Pearlite microstructure with interlamellar spacing and pearlite colony sizes of 80 ± 30 nm and 15 ± 5 μm was observed. Nanometric interlamellar spacing coupled with a thinning of the lamellar cementite causes relatively homogenous ductility with a low shear-cracking tendency [27]. It is worth-mentioning that in this steel, the work hardening behavior and hardness are improved by refined pearlite microstructure with fine interlamellar spacing which restricted the dislocation movement [28]. Pearlite steels are widely used in industries where high wear resistance is required. This high resistance against wear is due to the fine interlamellar spacing observed in the microstructure of as-received steel. The softening mechanisms, including dynamic recrystallization/recovery, shear bands, and cementite
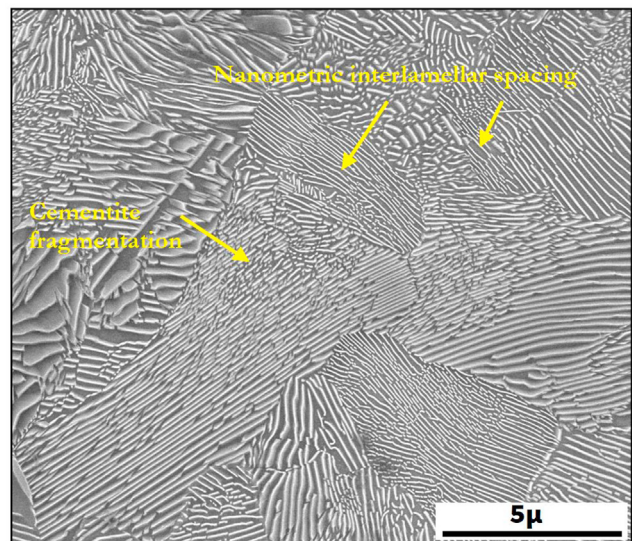
fragmentation during hot rolling (thermomechanical production processing) led to a reduction of mechanical strength due to the overall dislocation density reduction [29].

Fig. 3a and b shows the change in length vs temperature in Q&P treated specimens called as Q&P-220-325 and Q&P-220-375. These figures were provided in order two justify why such special temperatures were chosen for Q&P process. With the increase of temperature up to $A_{c1} = 780$ °C, the length is increased; however, in a point, a contraction occurred. This contraction shows that a transformation from the BCC ferrite to FCC austenite is occurred. When both specimens are cooled, the total phases consist of martensite and bainite. The above-mentioned phenomena were also shown in Fig. 3a and b. As shown in both diagrams, first, the length of specimens was increased with the increase of temperature. In some special regions, the length of specimens does not change with time. It is shown that the martensite start temperature (M_S) for both specimens are 267 °C. Both steels are cooled fast in order to form martensite, however, the objective is not to get 100% martensite. In other words, it is designed to generate approximately 50% martensite, while the rest remains as untransformed austenite. The austenite phase with FCC structure has four atoms in its crystal lattice and when it is transformed to the body-centered tetragonal (BCT) martensite with two atoms in its crystal lattice, an expansion would occur during such displacive transformation. After such expansion, the both specimens are subjected to the partitioning process at 325 °C and 375 °C to enhance bainitic transformation on remaining austenite as well as carbon partitioning from saturated martensite into surrounded austenite. The kinetics of isothermal bainitic transformation was designed at two different temperatures to investigate the possible development of different bainite formation. It is expected that a relatively higher supper-cooling (lower bainite transformation) is more favorable to reined bainitic sheaves and less carbon partitioning distance in medium carbon-silicon steel [30]. The thickness of bainite sheaves is determined by
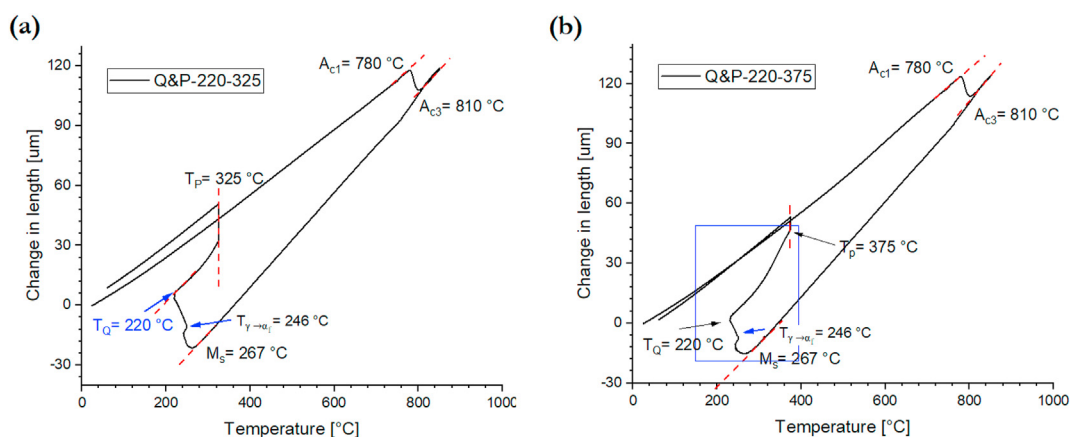
Fig. 3 — Change in length vs temperature in (a) Q&P-220-325 and (b) Q&P-220-375 investigated specimens.

the free energy change accompanying by transformation, governed by isothermal bainite transformation. A larger amount of dislocation and crystallographic defects under quenching lower than M_s, subsequently at lower bainitic transformation, promoted finer bainitic sheaves nucleation and contributed to the refinement of the resulting micro-structure and higher strength as well. Here, a transformation occurs with tempered martensite and bainite, while carbide particles and/or retained austenite (RA) particles could be developed according to the austenite stability. In other words, 50% of austenite transformed to bainite at the partitioning stage.

Predominant high dislocation structure as lath-like martensite microstructure developed after quenching below M_s temperature. However, autotempering-induced carbon redistribution from clustering to carbide precipitation is already initiated during quenching temperature at 220 °C, between M_s and M_f temperatures. During auto-tempering at the quenching step, carbon atoms could diffuse out of the interstitial martensite lath, generating carbon-vacancy defects due to the local extension into carbon clusters [31]. Morsdorf et al. [31] reported that plate-like martensite lattice formed parallel to (100) martensite lath with the least atomic density in the as-quenched state due to the maximum carbon compositions. Thereby, simultaneous poor and carbon-rich dislocation cores developed in microstructure, causing a lateral expansion in martensite plate sizes. By increasing the temperature to 246 °C, a small amount of lower stable austenite transformed into martensite, called newly formed martensite, probably due to the poor local carbon and man-ganese chemical composition variation, as reported by Grajcar et al. [32].

Fig. 4 shows the SEM micrographs of resulting Q&P-220-325 and Q&P-220-375 investigated specimens. As shown in these images, the microstructure of both specimens consists of a dispersion of ultrafine carbide through tempered martensite and bainitic sheaves. The carbon partitioning from saturated martensite to develop nanoscale carbide particles reduced the tetragonality of martensite, resulting in ductile BCC tempered martensite. Ultrafine carbide particles also generate enor-mous BCC matrix—carbide interfaces that act as effective sites against dislocation movement and grain sliding, enhancing

mechanical strengthening. Moreover, mainly lower bainite sheaves as carbide particles through the bainitic lath could exhibit a good combination of strength and ductility. A refined martensite/bainite microstructure was developed in Q&P-220-325 in comparison with Q&P-220-375 specimens, due to the lower partitioning temperature. It is also very difficult to distinguish the bainite microstructure from the tempered martensite since their SEM images are very similar. However, the hardness value of bainite is less than the tempered martensite and higher than the pearlite microstructure. Hardness measurements showed 565 ± 20 HV and 525 ± 20 HV of Q&P-220-325 and Q&P-220-375 specimens, respectively. The higher hardness of Q&P-220-325 specimen could be associated with the finer bainite sheaves and finer carbide dispersion through the martensite/bainite lath. Athermal saturated martensite formed under the quenching step gradually re-duces its tetragonality due to carbon atoms diffusion out to surrounded austenite. The stable enriched carbon untrans-formed austenite generated enhances bainitic transformation at the partitioning stage at higher temperatures than the bainite starts temperature. Bainite sheaves are composed of ferritic-bainite sheaves, and carbide particles originated from the remaining untransformed austenite at the quenching step, then transformed into bainitic sheaves at the isothermal partitioning stage. The martensite/austenite blocks are composed of the newly formed martensite and stable retained austenite also distrusted through resulting tempered martensite and bainitic structure, due to considerable amount of silicon (1.56 wt.%) by carbide-suppressing effect.

Fig. 5 shows the obtained XRD pattern for the original and quenched & partitioned specimens. It is shown the presence of $5 \pm 2\%$ of retained austenite of Q&P-220-325. In contrast, their peaks disappeared in Q&P-220-375 specimen due to the retained austenite decomposition. Moreover, a noticeable peak broadening for Q&P specimens could be associated with martensite tetragonality (c/a ration), critical nucleus size, and crystal defect densities. Comparison between the peak posi-tions and peak broadening reveals the martensite carbon depletion, reducing the peak broadening and shifting to higher angles to the original position of BCC ferrite peaks. Fig. 5b shows the variation of critical nucleus size (crystalline size), c/a ratio, and crystal defect density in all investigated
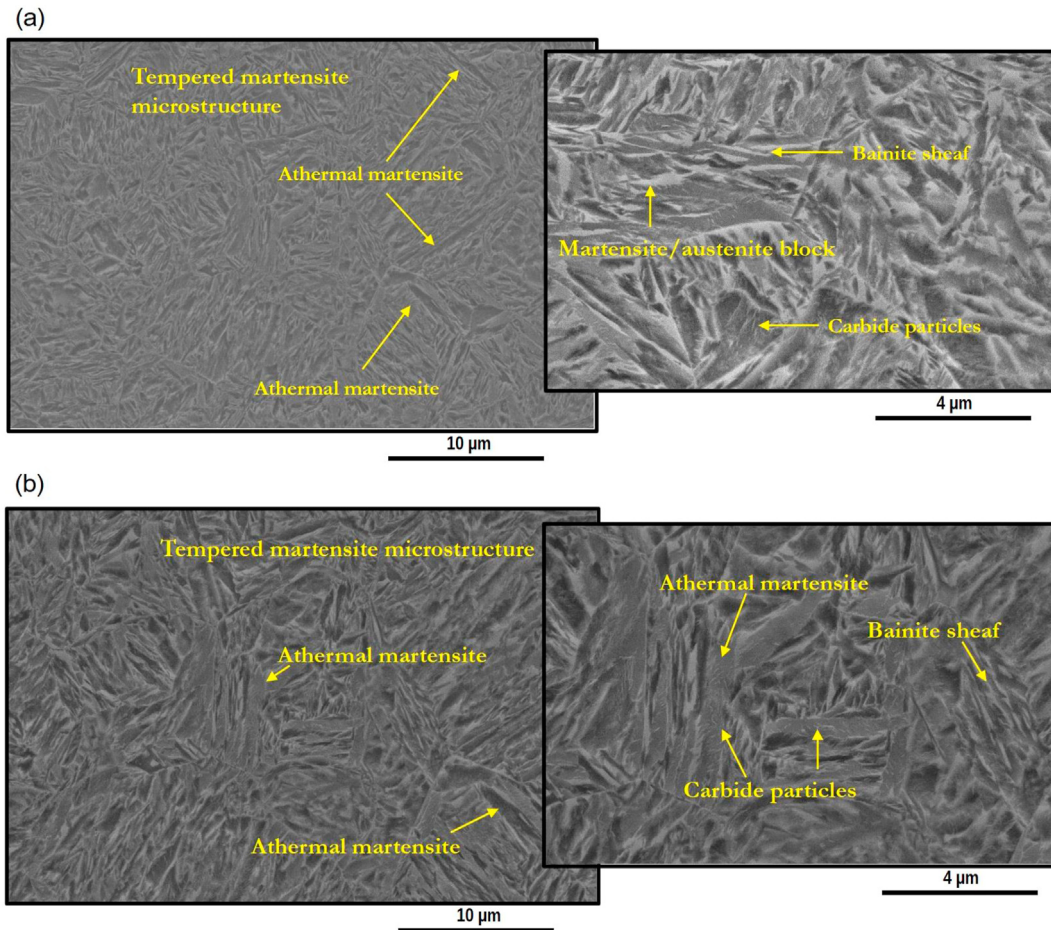
Fig. 4 — SEM micrographs of (a) Q&P-220-325 and (b) Q&P-220-375 specimen.

specimens. It is notably that critical nucleus size is associated with the nucleation of new particles from an untransformed solid solution, and strongly depends on super-cooling [18]. The lattice parameters of BCC lattice (martensite and bainite phases) are affected by carbon atoms, then carbon atoms migrate to the out of remaining austenite during the partitioning stage, especially at 375 °C. Saturated martensite developed in Q&P-220-325 specimens with a higher
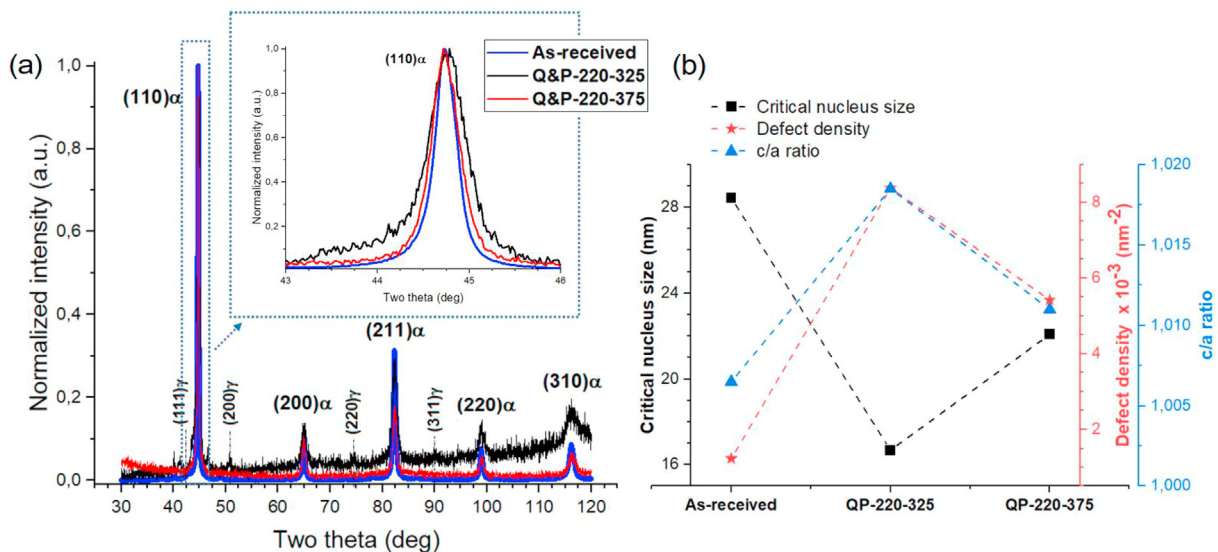

Fig. 5 — (a) XRD patterns and (b) variation of critical nucleus size, defect density, and c/a ratio obtained from corresponding XRD pattern of the investigated specimen.
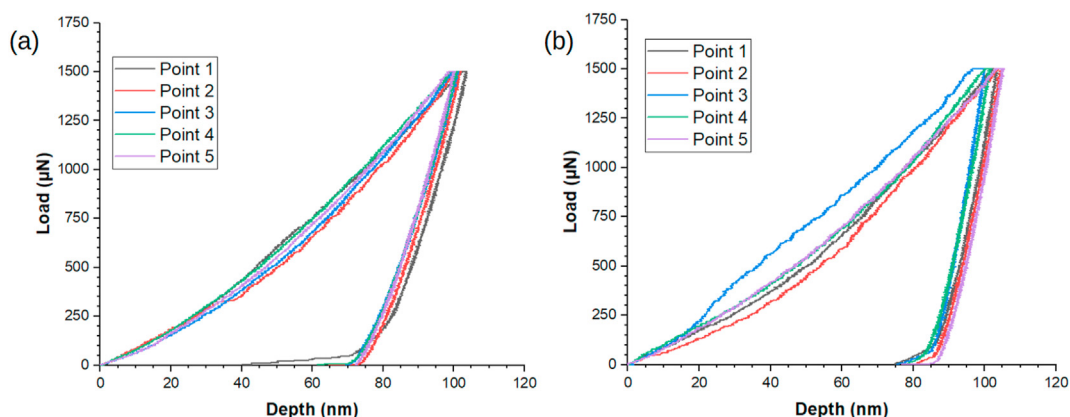
Fig. 6 – Load-displacement curves for (a) Q&P-220-325 and (b) Q&P-220-375 specimens.

tetragonality (c/a = 1.0185) is calculated in the specimen, causing a higher lattice distortion. Then, increasing the partitioning temperature and enhancing the carbon diffusion rate, the tetragonality reduced to (c/a = 1.0115), reducing the crystal defect. The partitioning rate of carbon results in rapid martensite carbon depletion and enhances the ferritic bainite phase transformation of the untransformed austenite.

Nanoindentation tests were performed to analyze the mechanical response of designed ultrafine multicomponent phases, corresponding to the load–displacement curves, presented in Fig. 6 in both treated specimens. The average nanohardness values of the Q&P-220-325 sample was 6.97 ± 0.30 GPa, while Q&P-220-375 samples exhibited less nanohardness, approximately 6.36 ± 0.25 GPa. It could be explained by the higher partitioning temperature, which led to partial nano carbide dissolution and higher carbon partitioning, which caused lower hardness compared to Q&P-220-325 sample.

Fig. 7a is a high-resolution SEM image of the Q&P-220-325 sample. The nanometer carbide particles are located within the bainitic sheaves (lower bainite). The micron-size film-like retained austenite is located at lath–lath interfaces. It is expected that dense dislocation tangles formed during partitioning by decomposition of retained austenite into nanoscaled carbide and bainite sheaves [21]. Although needle-like nanoscaled carbides are usually accompanied by dislocation tangles, increasing the partitioning temperature to

375 °C, some needle-like nanoscaled carbides dissolved and carbide coarsened at the lath–lath interface occurs, as shown in Fig. 7b for the Q&P-220-375 sample. It should be pointed out that EBSD can characterize the crystallographic characteristic of multiphase microstructure and determine the proportion of low and high angle boundaries to find the correlation between partitioning temperature of carbides dissolution and carbide coarsening on BCC matrix.

Fig. 8a–d shows the normal direction orientation imaging microscopy (OIM) map, orientation distribution function (ODF) and inverse pole figure (IPF), Kernel Average Misorientation (KAM) map and Taylor factor map for Q&P-220-325 specimen. According to Fig. 8a, the OIM map shows that most BCC matrix grains are aligned to {111}//ND orientations. Displacive phase transformation occurs at the operating slip system for each prior austenite grain. Martensite lath and ferritic-bainite sheaves directionally aligned along 111_{γ} plane as primary slip planes [17]. However, the diffusion mode bainitic transformation prompts the growth of the bainite sheaves along with other directions. It could be noted that <111> direction in BCC lattice as the most atomic compact direction can provide required slip planes to act as the preferential sites of bainite sheaves. Fig. 8b also shows the ODF map and IPF which was provided from the specimen, revealed the predominance of $(111)[1\bar{2}1]$ texture orientation. The presence of this crystallographic texture would cause high impact energy as it enhances fracture toughness due to the
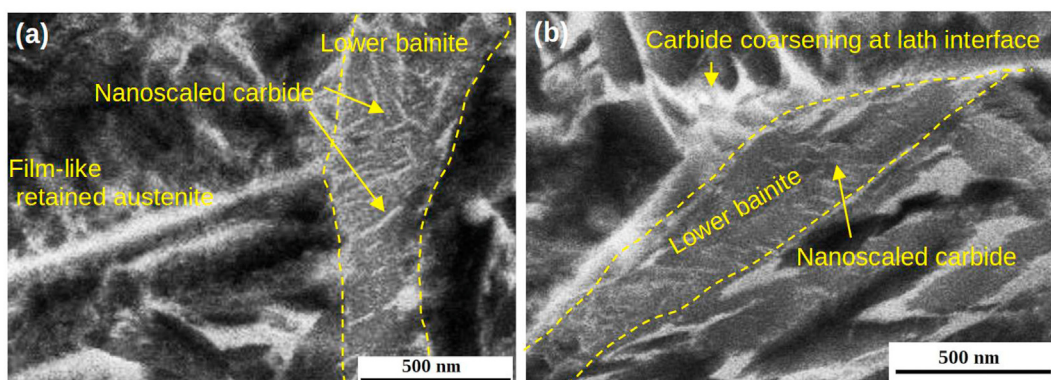

Fig. 7 – **High-resolution SEM image of the (a) Q&P-220-325 and (b) Q&P-220-375 specimens.**
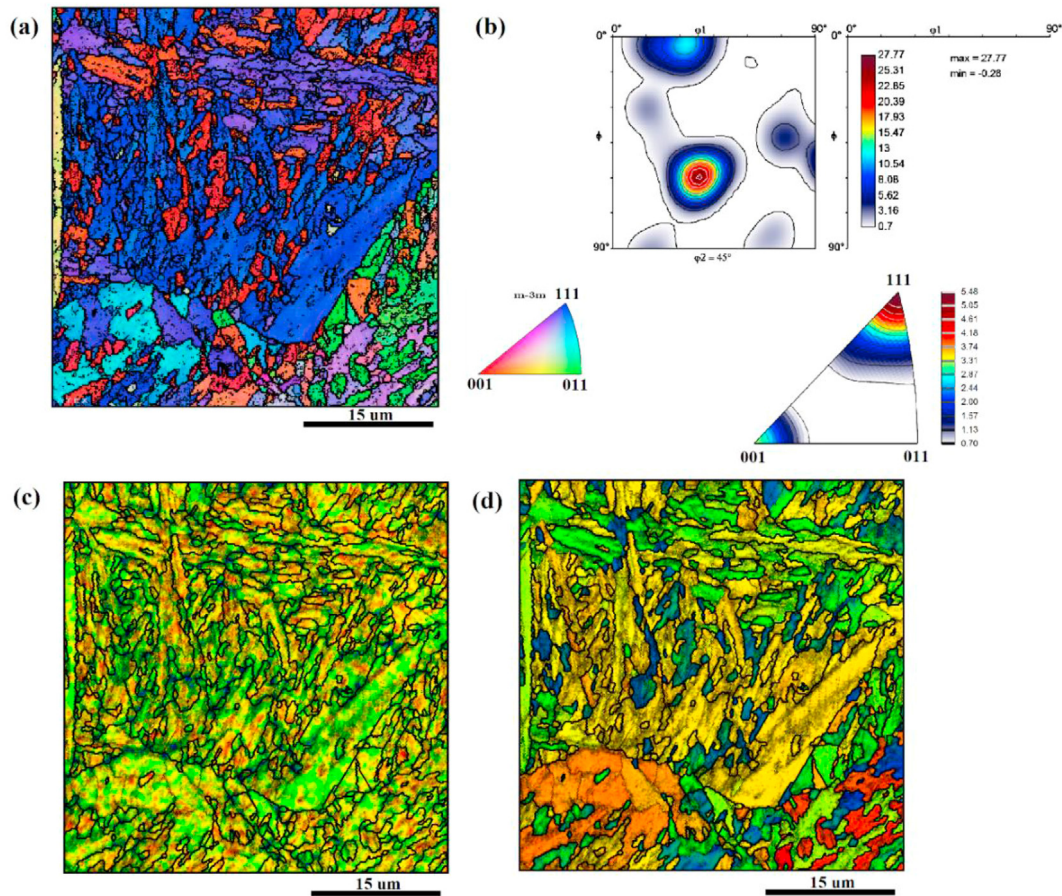
Fig. 8 — EBSD data for Q&P-220-325 specimen (a) OIM, (b) ODF and IPF map, (c) KAM and (d) Taylor factor map.

nucleation of the martensite from the stacking faults, formed by the partial dislocation $(a6)[112]$ at low strain [16]. It is worth-mentioning that in order to have a good statistic about the texture, it was better to measure the macro-texture using X-ray diffraction technique; however, it was the beyond the main objective of the current research. Fig. 8c shows the KAM map in the Q&P-220-325 specimen. KAM is utilized to show the average misorientation between a point and its nearest neighbors belonging to the same grain [33] to reveal the local strain accumulation. KAM is associated with a misorientation less than 5° and as a result, the Kernel map is able to evaluate the local plastic strain in steel materials [34]. In the interphases, the distortion is high and these regions are shown with red color. At the middle of BCC lath-like bainite (misorientation less than 15°), the localized strain is lower and these regions are shown with bright colors in Kernel map. According to Fig. 8d, Taylor factor map, the Taylor data for this specimen is almost low, indicating the high grain reorientation tendency. A Taylor factor is often used in order to express a flow stress measured in a polycrystal in terms of the critical resolved shear stress. Moreover, Taylor factor analyzes the level of plastic deformation of polycrystalline materials and presents distribution of the grain orientation showing a relation between the texture and yield stress [35,36]. In metals, soft grains are not initially oriented in a direction for slip occurring on slip planes. In such grains, the critical resolved shear stress is not easily achieved. In order to attain the critical resolved shear stress, the (111) martensite/bainite-laths should undergo some slight rotations to bring the slip planes into a new position [37]. According to Fig. 8d, since the Taylor factor data are low, further straining occurs in a difficult manner in this specimen. Thereby, since most grains have aligned along with <111>//ND orientations, the specimen can reorient and glide to accommodate mechanical stress, improving the fracture toughness.

Fig. 9a and b shows geometrically necessary dislocation (GND) density and Schmic factor maps for the Q&P-220-325 specimen. GND density shows gradients of plastic slip which is induced during plastic deformation [38,39]. In Fig. 9a, the regions with a high dislocation densities are shown with red color, however, the regions with a low dislocation density are shown with blue color. The GND value in the vicinity of martensite/bainite laths interfaces is the highest due to crystallographic defect densities and misfit between neighboring pixels. Moreover, the GND pile up reflects the variant selection at irrational oriented α/γ interfaces during martensitic phase transformation. It implies that plastic zone accumulated at these sites could deteriorate mechanical properties by forming pre-mature micro-cracks nucleation. The tangled dislocation induced during quenching stage, and further bainitic phase transformation, increased the dislocation density at remaining austenite and α/α interfaces. The average dislocation density is estimated approximately 5.67×10^{14} m^{-2}. Grain boundaries and tangles of dislocations
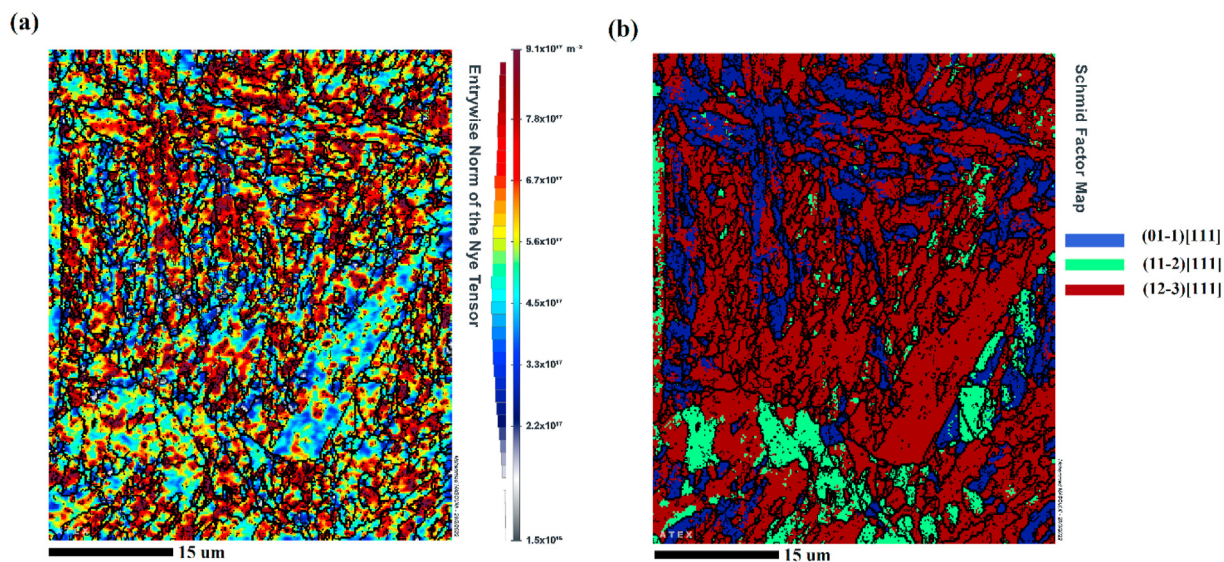
Fig. 9 — (a) GND density and (b) Schmid factor for Q&P-220-325specimen.

formed by rapid cooling increase the lattice distortion and internal energy. This phenomenon leads to an increase of nucleation rate of the bainitic transformation and reduce the incubation time to complete the bainitic transformation [40,41]. According to Fig. 9a, the dislocation density is high in the Q&P-220-325 specimen showing that there is a high amount of stored energy of deformation in this specimen. Moreover, during the applied Q&P heat treatment, the entire dislocation annihilation was not achieved. In other words, a higher amount of temperature or more time are required to get strain-free specimen. Fig. 9b shows the Schmid factor map for this specimen to reveal the dominant slip plane in each martensite/bainite BCC laths. Schmid factor describes the activated slip plane and the slip direction of a material which is under stress. It also dictates the amount of shear stress on a specific slip system due to the applied loading. It is obvious that the main slip system is the system with the highest Schmid factor. According to Fig. 9b, the Schmid factor map for Q&P-220-325 specimen, the slip occurs along the $(12\bar{3})[111]$, $(11\bar{2})[111]$ and $(01\bar{1})[111]$ planes and orientations. In martensite phase transformation, dislocation slip takes place in austenite phase during the transformation, and after the dislocation slip or twin shearing, FCC becomes BCC. The dominant $(12\bar{3})[111]$ slip system could be consequence of subsequent phase transformation, resulting in martensite and bainite originated from prior austenite grain.

Fig. 10a–d shows OIM map, ODF and IPF map, KAM and Taylor factor map for Q&P-220-375 specimen. Fig. 10a reveals a considerable difference in crystallographic texture orientation in this specimen compared to Q&P-220-325 specimen. Set of $(112)[0\bar{2}1]$, $(001)[120]$, and $(110)[1\bar{1}1]$ crystal orientation of observed in the microstructure developed at higher bainitic transformation temperatures. Guo et al. [17] explained that activated slip planes acting as preferential sites of Widmanstatten ferrite, would become into the habit plane by plate coarsening. Thereby, the variant selection tendency becomes more obvious, contrary to what is observed in the case of Q&P-

220-325 specimen. It is speculative to judge about the dominant texture based on Fig. 10a, however, the OIM image and IPF map, as shown in Fig. 10b, shows a considerable amount of cleavage {001} orientation in the Q&P-220-375 specimen. Therefore, one can predict that the higher number of cleavage <001> grain boundaries could deteriorate mechanical properties by providing an easy crack propagation path [42–45]. Bainite and tempered martensite grains in packets and blocks were developed in the specimen, usually originating from their orientation relationship and grain boundary characteristics with their prior austenite grain. Moreover, the diffusional transformation on bainitic kinetics lead to an irrational orientation relationship, which remains unclear yet [46]. Wang et al. [46] reported that the displacive martensite matrix from globular austenite grains at the packet boundary perfectly obeys the Kurdjumov−Sachs (K−S) orientation relationship. Whereas only (001) bainite pole figure matches the K−S pattern, indicating the initial displacive nucleation, while no oblivious matches were found in bainitic sheaves. The overall KAM map indicates that Q&P-220-375 specimen had a lower dislocation accumulation than the latest due to the dynamic recovery, recrystallization, and dislocation annihilation by partitioning at a higher temperature. Taylor factor map exhibits a combination of low and high Taylor factor grains, which means that hard grains are neighbor to the soft grains and vice versa. It causes the generation of stress concentration sites and facilitates heterogeneous plastic deformation and consequently, nucleation of microcracks.

Fig. 11a shows the GND distribution of martensite/bainite laths. The GND value in the vicinity of the packet and lath interfaces was higher than that inside the lath. It indicates that interfaces and boundaries contained more induced dislocation and crystallographic defects than grain interior. This finding could also show that the bainitic transformation with coupled displacive-diffusion transformation mechanism exhibited the irrational-oriented α/γ interfaces rather than martensite laths with strong K−S variant selection. On the one hand, the
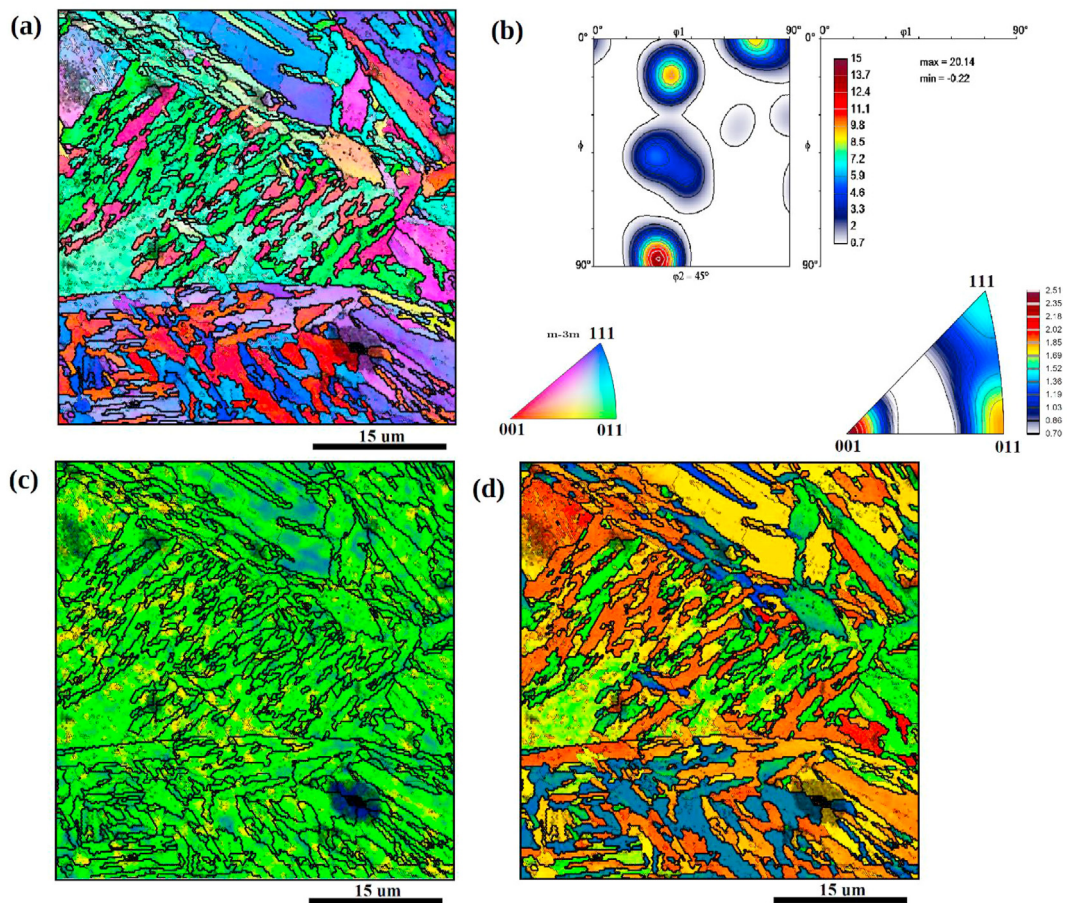
Fig. 10 − EBSD data for Q&P-220-375 specimen (a) OIM, (b) ODF and IPF map, (c) KAM and (d) Taylor factor map.

partitioning temperature at 375 °C enhanced the retained austenite decomposition into ultrafine carbide particles, and martensite-austenite blocks resulted in more intense strain accumulation sites. On the other hand, partial dynamic recovery, recrystallization, and dislocation annihilation reduced the amount of crystal defect densities. Therefore, the average dislocation density is estimated to be approximately $4.68 \times 10^{14} \, \text{m}^{-2}$ which is less than that in the case of Q&P-220-325 specimen. Fig. 11b shows the presence of activated slip systems on martensite and bainitic sheaves estimated by
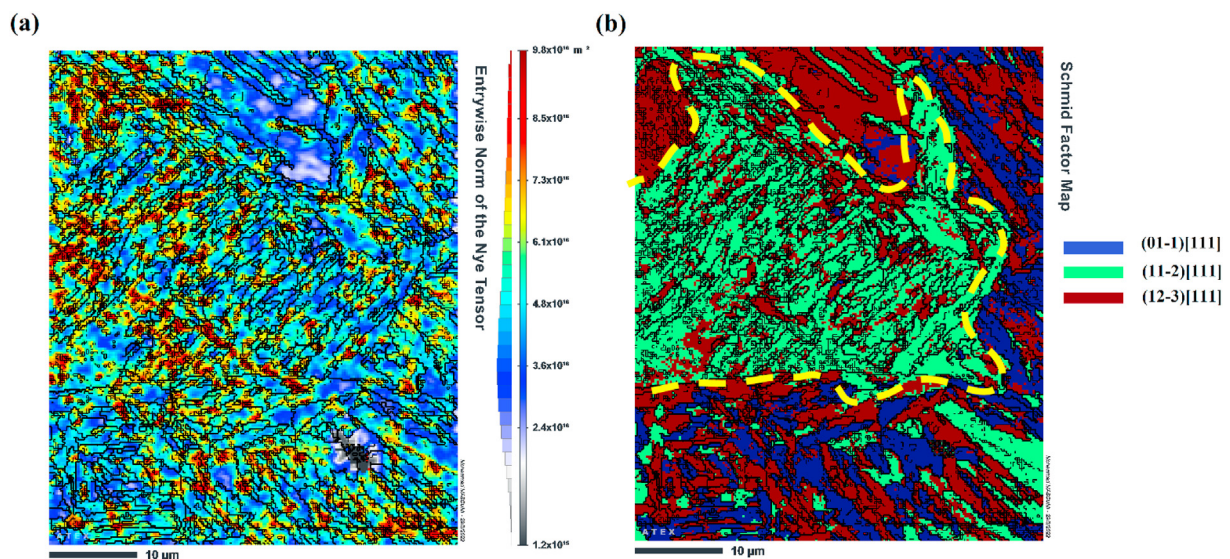

Fig. 11 − (a) GND density and (b) Schmid factor for specimen 2 (Q&P-220-375).
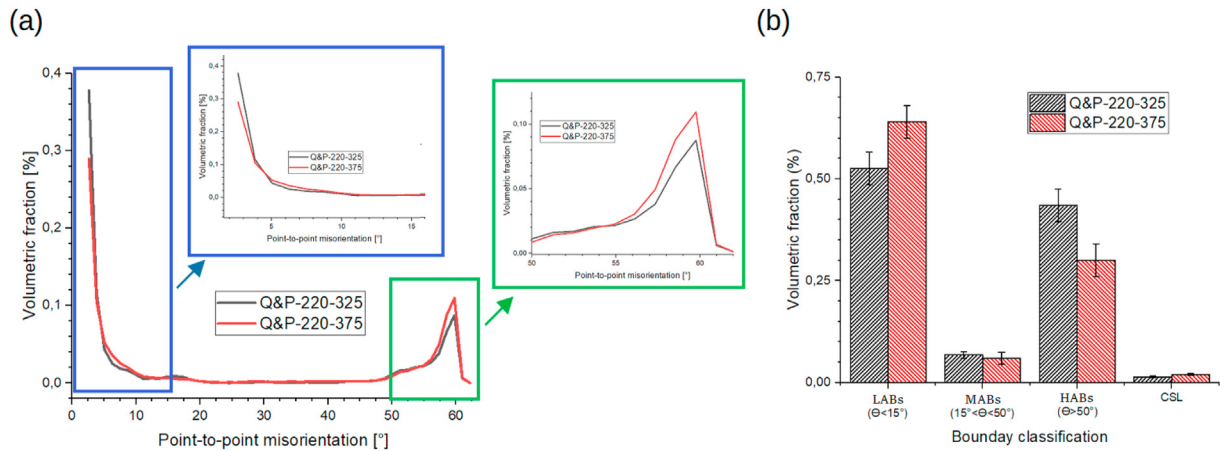
Fig. 12 – (a) Point-to-point misorientation and (b) grain boundary characteristics if investigated specimens.

Schmid factor undergo the plastic deformation due to the critical value of resolved shear stress during phase transformation [47]. Fig. 11b shows the predominant (112)[11 $\bar{1}$] slip system in a martensitic packet (yellow dash line) originated for the reconstructed prior austenite microstructure. This suggests that local plastic deformation induced by martensitic transformation locally activated the (112)[11 $\bar{1}$] slip system between prior austenite and product martensite. However, the change in activated slip systems between the other prior austenite grains could be explained by growth mechanism through diffusional-aid bainitic transformation [48].

Fig. 12a shows point-to-point misorientation in both designed and investigated specimens. This diagram shows that the volume fraction of low misorientations less than 5° is much higher than the misorientations range of 5°–50°. The volume fraction of misorientation higher than 50° increases again in both specimens. Fig. 12b also shows the grain boundary characteristics in both specimens, which are classified as low (LABs, θ < 15°), medium (MABs, 15° < θ < 50°), and high (HABs, θ > 50°) angle grain boundaries. Previous EBSD studies revealed that packed-lath martensite grain separated by high angular boundaries with high crystal defects due to

lattice distortion, while coarse-lath bainite sheaves separated by low and medium angular boundaries and possess high lattice defects as well [3,49,50]. Fig. 12b presents that the Q&P-220-325 specimen with a relative dominance of HABs could be associated with predominance martensite transformation, while Q&P-220-375 specimen demonstrates a slight dominance of LABs due to the bainitic sheaves formation and higher partitioning temperature. It is also noted that the volume fraction of coincidence site lattice (CSL) boundaries is negligible in the BCC matrix structure.

Two strengthening mechanisms, including dislocation and boundary strengthening, improve the mechanical strength by increasing the dislocation density and newly formed dislocation arrangement at ferrite boundaries and/or carbide-ferrite interfaces forming piling up, consequently acting as barriers against dislocation movement [29]. The KAM data analyses could better visualize the difference between BCC products by means of the intragranular average misorientation using a 5 × 5 Kernel reference accompanied with ignoring misorientation greater than 5° to eliminate the effect of subgrains [50]. Fig. 13a and b presents the distribution of Kernel data and grain's Kernel classification of
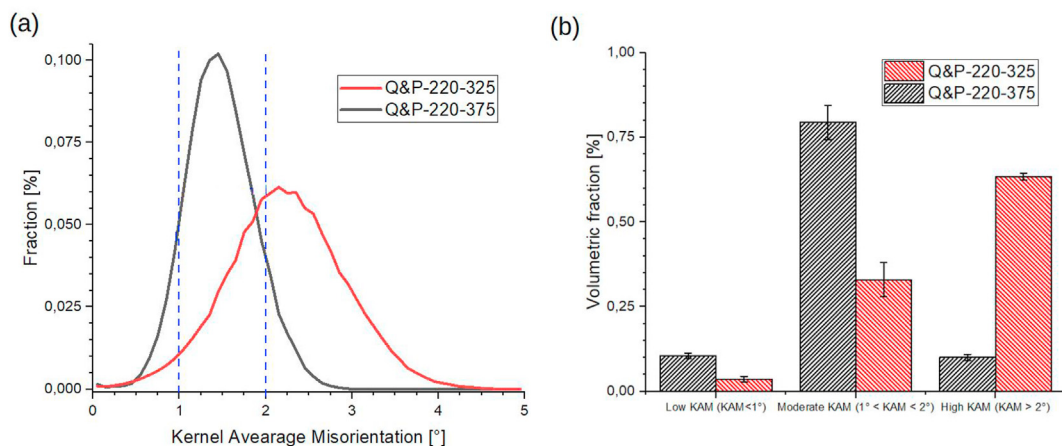

Fig. 13 – (a) Distribution of Kernel data and (b) Kernel classification of investigated specimens.

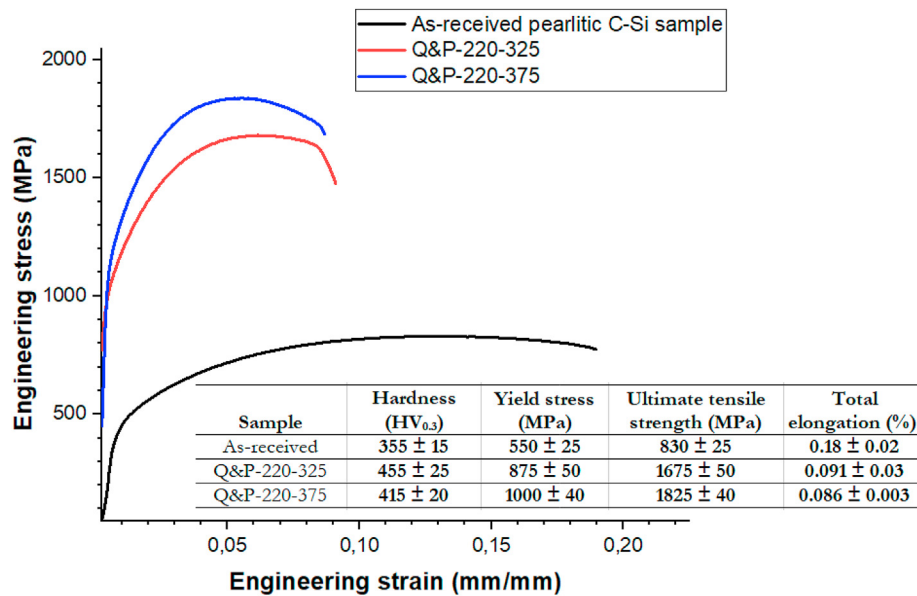| Sample	Hardness (HV$_{0.3}$)	Yield stress (MPa)	Ultimate tensile strength (MPa)	Total elongation (%)
As-received	355 ± 15	550 ± 25	830 ± 25	0.18 ± 0.02
Q&P-220-325	455 ± 25	875 ± 50	1675 ± 50	0.091 ± 0.03
Q&P-220-375	415 ± 20	1000 ± 40	1825 ± 40	0.086 ± 0.003

Fig. 14 — Engineering strain—stress curves, hardness and tensile properties of all investigated specimens.

investigated specimens. It is shown that the martensite dominance structure in Q&P-220-325 specimens had a more volume fraction of high KAM grains (KAM>2°). In contrast, the Q&P-220-375 specimen with a higher proportion of ferritic-bainite dominance structure due to higher partitioning temperature showed a higher fraction of moderate KAM grains (1° < KAM<2°). These findings agree with previous works that coarse sheaf bainite is identified with moderate KAM values. Moreover, lath-like displacive and diffusionless martensite is known for high local lattice distortion with a high defect density.

Fig. 14 shows the tensile test curves for the original as-received pearlitic C—Si steel, Q&P-220-325, and Q&P-220-375 specimens. The hardness, yield stress, and tensile strength were increased from the original as-received C—Si sample with pearlite structure to Q&P specimens by developing the complex microstructures. The quenching and partitioning process considerably increased the hardness and mechanical strength by a set of martensite and bainite structures coupled with nanoscale carbide or retained austenite particles. Results revealed that the development of nanoscale carbide dispersed in refined bainite/martensite matrix boosted the yield and ultimate tensile strength by over 100% and 110% compared to the initial pearlitic microstructure. The Q&P technology is quenching and carbon partitioning for high strengthened steels, which is intended to maintain high strength and increase plasticity by increasing the retained austenite during carbon partitioning. However, ductility reduced to half value in Q&P-220-325 and Q&P-220-375 specimens. A good ductility was obtained in the Q&P-220-325 specimen due to the dispersion of ultrafine retained austenite located at martensite lath, which probably enhanced ductility by transformation induced plasticity effect. It is known that displacive phase transformation leads to higher strength and lower ductility than diffusion phase transformation. Although our findings agreed with the mentioned statement, it is concluded that nanoscale retained austenite, martensite/austenite, and carbide particles can result in a good combination of strength and ductility gathering strengthening and ductility-enhancing mechanisms with transformation-induced plasticity effect and dislocation strengthening [19,51]. Moreover, the remaining ultrafine retained austenite and carbides surrounded by tempered martensite/bainite laths exhibited high mechanical stability in designed specimens originating from commercial pearlitic steel.

4.   Conclusion

In this research, the possibility of mechanical properties improvement of commercial pearlitic carbon-silicon steel by setting complex microstructures and crystallographic data (crystal orientation and boundary conditions) through quenching and partitioning process was investigated by different characterization techniques and tensile tests. The following points were concluded based on the experiments.

- Original pearlitic structure of commercial steel modified to a complex microstructures composed of tempered martensite, bainite, and nanoscale carbides/martensite-austenite/retained austenite particles.
- Resulting BCC matrix (martensite and bainite) exhibited a predominance <111> direction, which facilitates providing slip systems under further plastic deformation.
- Q&P-220-375 specimen had less crystallographic defect densities than Q&P-220-375 specimen, due to the partial dynamic recovery, recrystallization, and dislocation annihilation.
- Intense Taylor factor values variation in Q&P-220-375 specimen indicates the possibility of creation of the stress concentration especially at BCC lath interfaces.

- Point-to-point misorientation analyses demonstrated a slight dominance of low angle boundaries proportion in bainitic dominance structure in Q&P-220-375 specimen, which could be used in phase characterization.
- The average nanohardness values of the Q&P-220-325 sample was 6.97 ± 0.30 GPa, while Q&P-220-375 samples exhibited less nanohardness, approximately 6.36 ± 0.25 GPa due to the higher carbon partitioning.
- Development of nanoscale carbide dispersed in refined bainite/martensite matrix boosted the yield and ultimate tensile strength by over 100% and 110% compared to the initial pearlitic microstructure. However, ductility reduced to half value in Q&P-220-325 and Q&P-220-375 specimens.

Data availability statement

The experimental datasets obtained from this research work and then the analyzed results during the current study is available from the corresponding author on reasonable request.

Declaration of Competing Interest

The authors declare that they have no known competing financial interests or personal relationships that could have appeared to influence the work reported in this paper.

Acknowledgement

REFERENCES

[1] Maheswari N, Ghosh Chowdhury S, Hari Kumar KC, Sankaran S. Influence of alloying elements on the microstructure evolution and mechanical properties in quenched and partitioned steels. Mater Sci Eng A 2014;600:12—20.

[2] Speer J, Matlock DK, De Cooman BC, Schroth JG. Carbon partitioning into austenite after martensite transformation. Acta Mater 2003;51:2611—22.

[3] Ariza-Echeverri EA, Masoumi M, Nishikawa AS, Mesa DH, Marquez-Rossy AE, Tschiptschin AP. Development of a new generation of quench and partitioning steels: influence of processing parameters on texture, nanoindentation, and mechanical properties. Mater Des 2020;186:108329.

[4] Liu G, Zhang S, Li J, Wang J, Meng Q. Fast-heating for intercritical annealing of cold-rolled quenching and partitioning steel. Mater Sci Eng 2016;669:387—95.

[5] Zhu J, Ding R, He J, Yang Z, Zhang C, Chen H. A cyclic austenite reversion treatment for stabilizing austenite in the medium manganese steels. Scripta Mater 2017;136:6—10.

[6] Durgaprasad A, Giri S, Lenka S, Kundu S, Mishra S, Chandra S, et al. Defining a relationship between pearlite morphology and ferrite crystallographic orientation. Acta Mater 2017;129:278—89.

[7] Masoumi M, Béreš M, Herculano LFG, Loureiro RDCP, de Abreu HFG. Microstructure and crystallographic texture changes under torsion loading of pearlitic steel strips. J Mater Eng Perform 2020;29:7250—9.

[8] Loureiro RCP, Beres M, Masoumi M, de Abreu HFG. The effect of pearlite morphology and crystallographic texture on environmentally assisted cracking failure. Eng Fail Anal 2021;126:105450.

[9] Li ZX, Li CS, Zhang J, Li BZ, Pang XD. Microstructure of hot rolled 1.0c-1.5cr bearing steel and subsequent spheroidization annealing. Metall Mater Trans A 2016;47:3607—21.

[10] Lv ZQ, Wang B, Wang ZH, Sun SH, Fu WT. Effect of cyclic heat treatments on spheroidizing behavior of cementite in high carbon steel. Mater Sci Eng A 2013;574:143—8.

[11] Jia N, Shen YF, Liang JW, Feng XW, Wang HB, Misra RDK. Nanoscale spheroidized cementite induced ultrahigh strength- ductility combination in innovatively processed ultrafine-grained low alloy medium-carbon steel. Sci Rep 2017;7:2679.

[12] Grigorovich KV, Trushnikova AS, Arsenkin AM, Shibaev SS, Garber AK. Structure and metallurgical quality of rail steels produced by various manufacturers. Russian Metallurgy (Metally); 2006. p. 427—38. 2006.

[13] Moser A, Pointner P. Head-hardened rails produced from rolling heat. Transport Res Rec 1998;1341:70—4.

[14] Olofsson U, Zhu Y, Abbasi S, Lewis R, Lewis S. Tribology of the wheel-rail contact - aspects of wear, particle emission and adhesion. Veh Syst Dyn 2013;51:1091—120.

[15] Masoumi M, Ariza-Echeverri EA, Tschiptschin AP, Goldenstein H. Improvement of wear resistance in a pearlitic rail steel via quenching and partitioning processing. Sci Rep 2019;9:7454.

[16] Dong HY, Hu CY, Wu GH, Wu KM, Misra RDK. Effect of nickel on hardening behavior and mechanical properties of nanostructured bainite-austenite steels. Mater Sci Eng 2021;817:141410.

[17] Guo H, Feng X, Zhao A, Li Q, Chai M. Effects of ausforming temperature on bainite transformation kinetics, microstructures and mechanical properties in ultra-fine bainitic steel. J Mater Res Technol 2020;9:1593—605.

[18] Hosseini N, Forouzan F, Vuorinen E. In-situ microstructural evolution during quenching and partitioning of a high-carbon steel by high-temperature X-Ray diffraction. Mater Today Commun 2022;31:103503.

[19] Carvalho FM, Centeno D, Tressia G, Avila JA, Cezario FEM, Masoumi M. Development of a complex multicomponent microstructure on commercial carbon-silicon grade steel by governing the phase transformation mechanisms to design novel quenching and partitioning processing. J Mater Res Technol 2022;18:4590—603.

[20] Singh SB, Bhadeshia HKDH. Estimation of bainite plate-thickness in low-alloy steels. Mater Sci Eng 1998;245:72—9.

[21] Da Cruz Junior JA. Efeito do revenimento sobre a microestrutura e o desempenho mecânico de um aço multiconstituído com alto teor de Si. Universidade Federal De Minas Gerais Programa; 2014.

[22] Da Cruz Junior JA, Santos DB. Effect of tempering temperature on isothermal decomposition product formed below Ms. J Mater Res Technol 2013;2:93—9.

[23] Santos DB, Da Cruz Junior JA, Rodrigues TFM, Viana VDC. Bainite formation at low temperatures in high C-Si steel and its mechanical behavior. Mater Sci Forum 2012;706—709:173—80.

[24] Serbino EM, Tschiptschin AP. Fatigue behavior of bainitic and martensitic super clean Cr-Si high strength steels. Int J Fatig 2014;61:87—92.

[25] Beausir B, Fundenberger J-J. Analysis tools for electron and X-ray diffraction. ATEX - software. Université de Lorraine - Metz; 2017 [n.d.], www.atex-software.eu.

[26] Dragomir IC, Li DS, Castello-Branco GA, Garmestani H, Snyder RL, Ribarik G, et al. Evolution of dislocation density and character in hot rolled titanium determined by X-ray diffraction. Mater Char 2005;55:66—74.

[27] Liang LW, Wang YJ, Chen Y, Wang HY, Dai LH. Dislocation nucleation and evolution at the ferrite-cementite interface under cyclic loadings. Acta Mater 2020;186:267—77.

[28] Masoumi M, de Lima NB, Tressiac G, Sinatora A, Goldenstein H. Microstructure and crystallographic orientation evolutions below the superficial white layer of a used pearlitic rail. J Mater Technol 2019;8:6275—88.

[29] Zhao TZ, Zhang SH, Zhang GL, Song HW, Cheng M. Hardening and softening mechanisms of pearlitic steel wire under torsion. Mater Des 2014;59:397—405.

[30] Zou H, Hu H, Xu G, Xiong Z, Dai F. Combined effects of deformation and undercooling on isothermal bainitic transformation in an Fe-C-Mn-Si alloy. Metals 2019;9:138.

[31] Morsdorf L, Emelina E, Gault B, Herbig M, Tasan CC. Carbon redistribution in quenched and tempered lath martensite. Acta Mater 2021;205:116521.

[32] Grajcar A, Morawiec M, Jimenez JA, Garcia-Mateo C. Dilatometric and microstructural study of martensite tempering in 4% Mn steel. Materials 2020;13:4442.

[33] Badji R, Chauveau T, Bacroix B. Texture, misorientation and mechanical anisotropy in a deformed dual phase stainless steel weld joint. Mater Sci Eng A 2013;575:94—103.

[34] Mohtadi-Bonab MA, Eskandari M, Szpunar JA. Texture, local misorientation, grain boundary and recrystallization fraction in pipeline steels related to hydrogen induced cracking. Mater Sci Eng A 2015;620:97—105.

[35] Shen JH, Li YL, Wei Q. Statistic derivation of Taylor factors for polycrystalline metals with application to pure magnesium. Mater Sci Eng A 2013;582:270—5.

[36] Kocks UF, Mecking H. Physics and phenomenology of strain hardening: the FCC case. Prog Mater Sci 2003;48:171—273.

[37] Mohtadi-Bonab MA, Szpunar JA, Basu R, Eskandari M. The mechanism of failure by hydrogen induced cracking in an acidic environment for API 5L X70 pipeline steel. Int J Hydrog Energy 2015;40:1096—107.

[38] Dahlberg CFO, Saito Y, Öztop MS, Kysar JW. Geometrically necessary dislocation density measurements associated with different angles of indentations. Int J Plast 2014;54:81—95.

[39] Kysar JW, Saito Y, Oztop MS, Lee D, Huh WT. Experimental lower bounds on geometrically necessary dislocation density. Int J Plast 2010;26:1097—123.

[40] Long X, Zhang F, Yang Z, Zhang M. Study on bainitic transformation by dilatometer and in situ LSCM. Materials 2019;12:1534.

[41] Chen G, Xu G, Zurob HS, Hu H, Wan X. Effect of strain rate on the bainitic transformation in Fe-C-Mn-Si medium-carbon bainitic steels. Metall Mater Trans 2019;50:573—80.

[42] Ramirez MFG, Hernández JWC, Ladino DH, Masoumi M, Goldenstein H. Effects of different cooling rates on the microstructure, crystallographic features, and hydrogen induced cracking of API X80 pipeline steel. J Mater Res Technol 2021;14:1848—61.

[43] Pourazizi R, Mohtadi-Bonab MA, Szpunar JA. Role of texture and inclusions on the failure of an API X70 pipeline steel at different service environments. Mater Char 2020;164:110330.

[44] Masoumi M, Silva CC, Béreš M, Ladino DH, de Abreu HFG. Role of crystallographic texture on the improvement of hydrogen-induced crack resistance in API 5L X70 pipeline steel. Int J Hydrog Energy 2017;42:1318—26.

[45] Masoumi M, Silva CC, de Abreu HFG. Effect of crystallographic orientations on the hydrogen-induced cracking resistance improvement of API 5L X70 pipeline steel under various thermomechanical processing. Corrosion Sci 2016;111:121—31.

[46] Wang T, Qian L, Yu W, Li K, Zhang F, Meng J. Effect of ferrite-austenite morphology and orientation relationship on bainite transformation in low-alloy TRIP steels. Mater Char 2022;184:111656.

[47] Niessen F, Gazder AA, Hald J, Somers MAJ. Multiscale in-situ studies of strain-induced martensite formation in inter-critically annealed extra-low-carbon martensitic stainless steel. Acta Mater 2021;220:117339.

[48] Kim DW, Yang J, Kim YG, Kim W-K, Lee S, Sohn SS. Effects of granular bainite and polygonal ferrite on yield strength anisotropy in API X65 linepipe steel. Mater Sci Eng 2022;843:143151.

[49] Rementeria R, Jimenez JA, Allain SYP, Geandier G, Poplawsky JD, Guo W, et al. Quantitative assessment of carbon allocation anomalies in low temperature bainite. Acta Mater 2017;133:333—45.

[50] Breumier S, Martinez Ostormujof T, Frincu B, Gey N, Couturier A, Loukachenko N, et al. Leveraging EBSD data by deep learning for bainite, ferrite and martensite segmentation. Mater Charact 2022;186:111805.

[51] Zhang X, Teng R, Liu T, Shi Y, Lv Z, Zhou Q, et al. Improving strength—ductility synergy in medium Mn steel by combining heterogeneous structure and TRIP effect. Mater Charact 2022;184:111661.